14th International Symposium on Turbulence and Shear Flow Phenomena (TSFP14)
Heidelberg, Germany, July 28–31, 2026

HEAVY KOLMOGOROV-SIZE SPHERICAL PARTICLES IN HOMOGENEOUS ISOTROPIC TURBULENCE

Ludovico Fossà
Complex Fluids and Flows Unit
Okinawa Institute of Science and Technology Graduate University (OIST)
1919-1 Tancha, Onna-son, Kunigami-gun, Okinawa-ken 904-0495 Japan
Email ludovico-fossa@oist.jp, marco-rosti@oist.jp

Marco Edoardo Rosti
Complex Fluids and Flows Unit
Okinawa Institute of Science and Technology Graduate University (OIST)
1919-1 Tancha, Onna-son, Kunigami-gun, Okinawa-ken 904-0495 Japan
Email ludovico-fossa@oist.jp, marco-rosti@oist.jp

ABSTRACT

The impact of Kolmogorov-size spherical particles on homogeneous isotropic turbulence is examined through particle-resolved direct numerical simulations. Four monodisperse particle suspensions are analyzed, all sharing the same diameter and volume fraction, while the particle-to-fluid density ratio spans the range 100 to 1500 and the corresponding mass fraction varies from 0.1 to 0.6. With increasing particle inertia, the energy spectrum progressively deviates from the classical Kolmogorov $\kappa^{-5/3}$ scaling, tending instead toward an anomalous κ^{-1} behavior. In this regime, nonlinear energy transfer is significantly reduced, and the kinetic energy budget becomes primarily governed by fluid-solid coupling and viscous dissipation. In agreement with this observation, the second-order structure function exhibits logarithmic scaling for separations exceeding the particle diameter, which signals a loss of velocity correlation. Furthermore, the magnitude of the particle velocity follows a Gaussian distribution across all cases, while particle clustering diminishes as the density ratio increases.

INTRODUCTION

Particle-laden flows are widespread in both natural and industrial contexts. Representative examples include water droplets and ice crystals in atmospheric clouds, volcanic ash, dust in protoplanetary disks, sandstorms, ocean microplastics, blood cells, and fuel droplets in spray combustion. In such systems, a liquid or gaseous carrier flow transports and interacts with a dispersed phase that may be solid, liquid, or gaseous. The carrier phase is frequently turbulent, encompassing a wide range of spatial and temporal scales. The majority of numerical and experimental investigations of particle-laden turbulence have focused on spherical solid particles with diameters either much larger ($D \gg \eta$) or much smaller ($D \ll \eta$) than the Kolmogorov scale η. Suspensions composed of particles with size comparable to the Kolmogorov scale and with moderate-to-high volume fraction Φ_p are known to modify the bulk behavior of an otherwise single-phase turbulent flow (Schneiders *et al.*, 2017; Marchioli *et al.*, 2025). While the point-particle approximation has been widely adopted for cases with very small D/η, low volume fractions Φ_p, and moderate mass fractions Ψ_p, it is not suitable for many realistic configurations where resolving the flow in the vicinity of the particles is essential (Brandt & Coletti, 2022; Chiarini *et al.*, 2025). Conversely, particle-resolved direct numerical simulations (PR-DNS) entail substantially higher computational costs than single-phase or point-particle DNS, as the computational mesh must resolve sub-Kolmogorov flow features around each particle. Consequently, the influence of increasing particle inertia in suspensions with moderate-to-high volume fraction has received comparatively limited attention. In the present study, we investigate the role of particle inertia in the interaction between homogeneous isotropic turbulence and a monodisperse suspension of Kolmogorov-size spheres. Through large-scale PR-DNS, we analyze how variations in the particle-to-fluid density ratio impact the mechanical properties of the flow, the scale-dependent energy transfer, and particle clustering.

DIRECT NUMERICAL SIMULATIONS

We consider a triply periodic cubic domain of volume $\mathscr{V} = L^3 = (2\pi)^3$. The carrier phase is described by the incompressible Navier–Stokes equations

$$\partial_t u_i + \partial_j \left(u_j u_i\right) = \rho_f^{-1} \partial_j \sigma_{ij} + f_i^{\mathrm{ABC}} + f_i^{\mathrm{part}}, \qquad (1)$$

where Einstein summation over repeated indices is assumed. In this formulation, u_i denotes the fluid velocity, ρ_f the fluid density, and f_i^{part} the volumetric forcing exerted by the particles on the fluid (Hori *et al.*, 2022). The large-scale forcing term f_i^{ABC} follows the Arnold–Beltrami–Childress (ABC) formulation (Arnold, 1965, p. 20) with amplitude $F_0 = 5$. The Cauchy stress tensor σ_{ij} reads

$$\sigma_{ij} = -p\delta_{ij} + 2\mu_f S_{ij}, \qquad (2)$$

where p is the pressure, δ_{ij} the Kronecker delta, μ_f the dynamic viscosity, and $S_{ij} = (\partial_j u_i + \partial_i u_j)/2$ the symmetric part of the velocity gradient tensor $\partial_j u_i$. The evolution of the particle translational velocity $\tilde{U}_i$ and angular velocity Ω_i is governed by the Newton–Euler equations

$$\mathrm{d}_t \tilde{U}_i = m_p^{-1} \oint_{\partial \mathscr{V}_p} \sigma i j n_j \mathrm{d}(\partial \mathscr{V}) + F_i^{\mathrm{col}}, \tag{3a}$$

$$\mathrm{d}_t \Omega_i = \mathscr{I} p^{-1} \oint \partial \mathscr{V} p \varepsilon_{ijk} r_j \sigma k l n_l \mathrm{d}(\partial \mathscr{V}). \tag{3b}$$

Here, n_i denotes the outward unit normal to the particle surface, $m_p = (\pi/6)\rho_p D^3$ and $\mathscr{I}_p = (m_p/10)D^2$ are respectively the particle mass and moment of inertia, and D is the particle diameter. No-slip and no-penetration boundary conditions are imposed at the particle surface. The term F^{col} accounts for particle-particle interactions, modeled using the mass-spring-dashpot approach of Tsuji *et al.* (1993) and Costa *et al.* (2015). The numerical methodology outlined here is implemented in the in-house Fortran solver *Fujin* (Rosti, 2026). The fluid momentum equation (1) is integrated in time using a fractional-step scheme (Kim *et al.*, 1987; Tomé *et al.*, 1996), while phase coupling is handled through the Eulerian immersed boundary method (IBM) described by Hori *et al.* (2022). The triply periodic domain is discretized on a uniform Cartesian mesh with 2048^3 grid points, and all simulations are carried out using 4096 computational cores. We consider a monodisperse population of $N = 74\,208$ spherical particles with diameter $D \cong 0.003L$, corresponding to the Kolmogorov scale η in all configurations. The solid volume fraction is fixed at $\Phi_p = (\pi N/6)(D/L)^3 = 10^{-3}$ for all cases. Consequently, the mass fraction depends exclusively on the density ratio $\Psi_p = \rho_p/\rho_f$ according to

$$M_p = \Psi_p \Phi_p \left(1 - \Phi_p + \Psi_p \Phi_p\right)^{-1}. \tag{4}$$

Four particle-laden configurations are examined, with density ratios $\Psi_p = 100$, 250, 666, and 1499, corresponding to mass fractions $M_p = 0.1$, 0.2, 0.4, and 0.6. These are compared against the unladen reference case ($\Phi_p = M_p = 0$). The selected values of M_p are consistent with those reported in the experiments of Tanaka & Eaton (2010) (see table 3 therein).

RESULTS

Statistics of the carrier flow

An increase in the inertia of Kolmogorov-size particles produces a pronounced modification of the mechanical properties of the turbulent carrier flow. Spatial averages over the domain $\langle\cdot\rangle_{\mathscr{V}}$, temporal averages $\langle\cdot\rangle_t$, and combined space–time averages $\langle\cdot\rangle_{\mathscr{V},t} = \langle\langle\cdot\rangle_{\mathscr{V}}\rangle_t$ are evaluated, with the corresponding values reported in table 1, where the four particle-laden configurations are compared against the unladen reference case $M_p = 0$. The kinetic energy is defined as $K = u_i u_i/2$, while the dissipation rate, introduced earlier, is $\varepsilon = 2\nu_f S_{ij} S_{ij}$. The Kolmogorov length scale is $\eta = (\nu_f^3/\langle\varepsilon\rangle_{\mathscr{V}})^{1/4}$ and the associated time scale is $(\nu_f/\langle\varepsilon\rangle_{\mathscr{V}})^{1/2}$. The longitudinal Taylor microscale is given by $\lambda = (20\nu_f \langle K\rangle_{\mathscr{V}} / \langle\varepsilon\rangle_{\mathscr{V}})^{1/2}$, and the corresponding Reynolds number is $Re_\lambda = u_{\mathrm{rms}} \langle\lambda\rangle_{\mathscr{V}} / \nu_f$, where $u_{\mathrm{rms}} = (2\langle K\rangle_{\mathscr{V}}/3)^{1/2}$ denotes the root-mean-square velocity.

The quantities $\langle K\rangle_{\mathscr{V},t}$, $\langle\varepsilon\rangle_{\mathscr{V},t}$, and $\langle Re_\lambda\rangle_t$ all exhibit a clear reduction with increasing M_p. This behavior reflects the fact that a substantial fraction of the turbulent kinetic energy is directly transferred to the suspension through the fluid-particle coupling term f_i^{part} in (1) and the surface integrals appearing in (3). In contrast, the Kolmogorov length scale η does not show any appreciable dependence on M_p, thereby confirming that $D \cong \eta$.

Ψ_p	M_p	$\dfrac{\langle K\rangle_{\mathscr{V},t}}{F_0 L}$	$\dfrac{\langle\varepsilon\rangle_{\mathscr{V},t}}{(F_0^3 L)^{1/2}}$	$\langle Re_\lambda\rangle_t$
-	0	2.11	2.40	149.34
100	0.1	1.60	1.89	127.29
250	0.2	1.47	1.83	117.94
666	0.4	1.42	2.03	108.57
1499	0.6	1.42	2.07	107.58

Table 1: Statistics of the carrier flow. The first row describes the unladen case and the others the laden cases. All the quantities are non-dimensional. The space-time average of the kinetic energy $\langle K\rangle_{\mathscr{V},t}$, the space-time average of the dissipation rate $\langle\varepsilon\rangle_{\mathscr{V},t}$ and the time average Taylor-based Reynolds number $\langle Re_\lambda\rangle_t$ are listed.

These observations are consistent with the experimental results of Tanaka & Eaton (2010), who reported a 25% reduction in the mean turbulent kinetic energy when a homogeneous isotropic turbulent flow at $Re_\lambda \cong 130$ was seeded with Kolmogorov-size particles characterized by $D/\eta \cong 2$, $M_p = 0.4$, and $\Phi_p = 1.8 \times 10^{-4}$ (see figure 16 therein). In the present direct numerical simulations, a reduction of 32% in $\langle K\rangle_{\mathscr{V},t}$ is measured when an initially unladen turbulent flow at $Re_\lambda \cong 150$ is loaded with a suspension of volume fraction $\Phi_p = 10^{-3}$ and mass fraction $M_p = 0.4$.

The flow visualizations in figure 1 show the effect of M_p (and Ψ_p) on the dissipation rate $\varepsilon = 2\nu_f S_{ij} S_{ij}$. Here, regions of low and high dissipation are drawn in dark blue and dark orange, respectively. All the cases show large excursions in ε. While large turbulent structures are still present in the case with the lowest mass fraction (figure 1, left), the peaks of large ε become confined to the particles' shear layers as M_p increases (figure 1, right). The large regions of high ε have vanished: the flow field is characterised by smaller, adjacent regions of moderate (yellow) and low (blue) ε, while the dissipation remains still elevated in the particles' wakes.

Kinetic energy spectra

To elucidate the influence of the dispersed phase on the scale-wise distribution of turbulent kinetic energy, we compare the energy spectra $\hat{E}(\kappa)$ for different values of the mass fraction M_p. The corresponding results are presented in figure 2 (left). As M_p increases, the spectra progressively deviate from the classical Kolmogorov $-5/3$ scaling. At the same time, a slight enhancement of kinetic energy is observed at the smallest resolved scales ($\kappa/\kappa_L > 10^2$). Kolmogorov-size particles thus attenuate the large-scale structures while promoting small-scale fluctuations at wavenumbers comparable to or exceeding the particle wavenumber L/D. A similar trend has been previously documented in decaying isotropic turbulence (Schneiders *et al.*, 2017, see figure 7 therein). The behavior of $\langle\hat{E}\rangle_t$ is consistent with the qualitative picture in figure 1, where regions of intense dissipation become increasingly localized in particle wakes as the density of the dispersed phase grows.

For the case with the largest particle inertia (brown curve

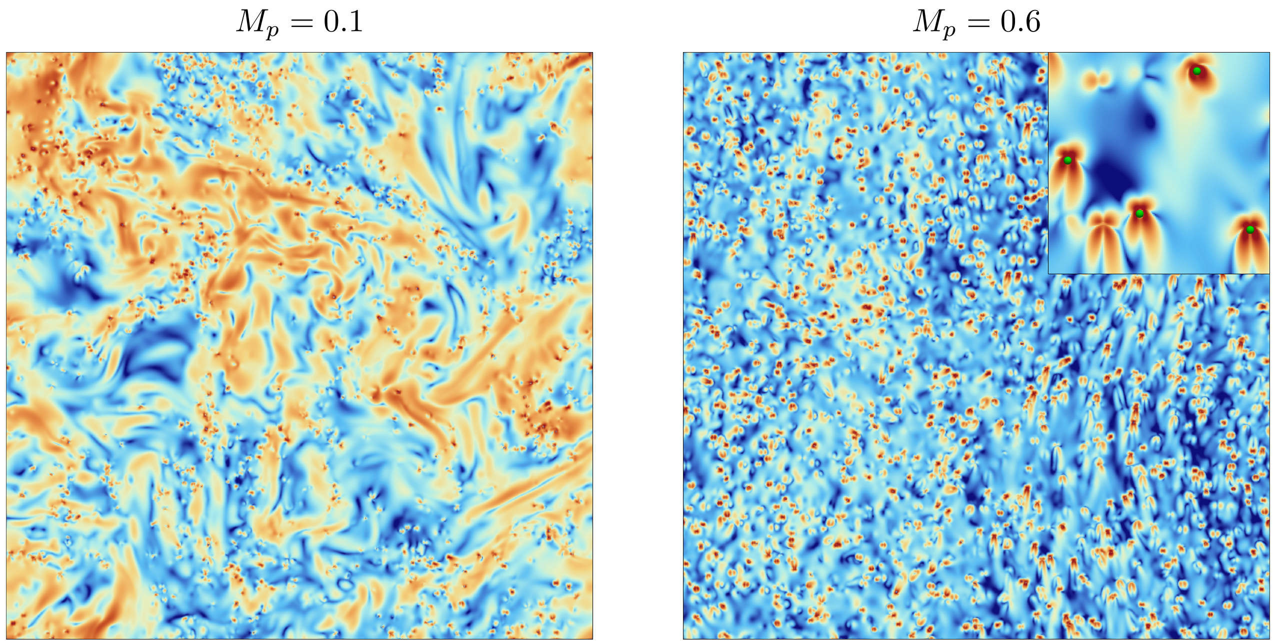

Figure 1: Instantaneous visualization of the turbulent kinetic energy dissipation rate $\varepsilon = 2\nu_f S_{ij} S_{ij}$. Regions of low and high dissipation are drawn in shades of blue and red, respectively. The mass fraction of the particles is $M_p = 0.1$ (left) and 0.6 (right). The inset provides a zoomed view of the flow field at the particle scale (green particles).

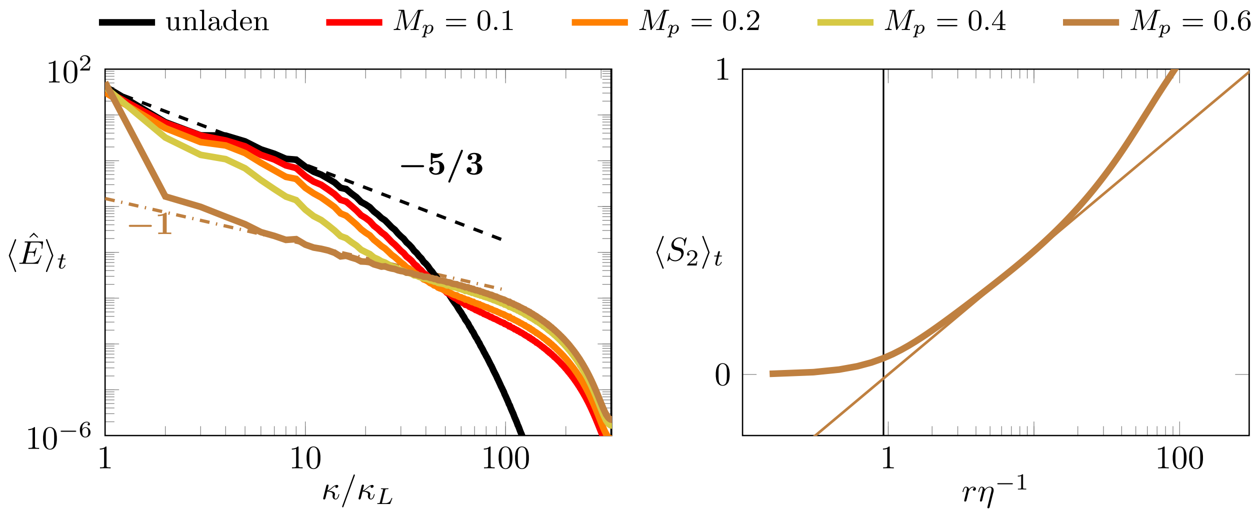

Figure 2: Left: kinetic energy spectra $\langle \hat{E} \rangle_t$ for increasing mass fraction M_p of the particles. The black dashed line and the brown dash-dot line the $(\kappa/\kappa_L)^{-5/3}$, $(\kappa/\kappa_L)^{-1}$, respectively. Right: second-order longitudinal structure function $\langle S_2 \rangle_t$ features a logarithmic scaling for separations $r > \eta$ (brown line). The black vertical line in denotes the particle diameter $D \approx \eta$.

in figure 2, left), the energy spectrum exhibits a $(\kappa/\kappa_L)^{-1}$ scaling over the interval $2 \leq \kappa/\kappa_L < 70$ (brown dash-dot line). An analogous scaling has been reported by Olivieri *et al.* (2022*a*) in turbulent flows laden with slender fibres of Kolmogorov-size cross-section. In that work, it was suggested that sufficiently heavy fibres act as barriers between points separated by distances larger than the fibre thickness, thereby inducing flow decorrelation and altering both the exponent of the second-order structure function and the spectral scaling of $\langle \hat{E} \rangle_t$. To determine whether a comparable mechanism is at play for heavy Kolmogorov-size particles, we evaluate the second-order longitudinal structure function of the carrier flow, $S_2(r) = \langle [\delta u(r,t)]^2 \rangle_{\mathscr{V}}$, where $\delta u(r,t) = [u(x+r,t) - u(x,t)] \cdot r/|r|$ denotes the longitudinal velocity increment (Pope, 2000, §6.7.2). Figure 2 (right) reports a semi-logarithmic representation of the second-order structure function (thick curve), together with $\log(r/\eta)$ over the range $1 \leq r/\eta < 10^2$. In homogeneous isotropic turbulence, the asymptotic behavior $\langle S_2 \rangle_t \sim \log(r/\eta)$ for $r\kappa \gg 1$ is consistent with a spectral scaling $\langle \hat{E} \rangle_t \sim \kappa^{-1}$. Furthermore, the saturation of S_2 indicates a breakdown of velocity autocorrelation (Pope, 2000, §6). Altogether, these results suggest that heavy Kolmogorov-size particles induce local decorrelation of the turbulent velocity field over separations larger than the particle diameter D.

Scale-by-scale energy transfer

The individual contributions in the kinetic energy balance equation offer further insight into how the dispersed phase modulates the carrier flow. When expressed as functions of the spatial wavenumber κ, these terms enable a scale-resolved assessment of energy production, transfer, and dissipation. They are obtained by contracting the Fourier transform of the momentum equation (1) with the Fourier-transformed velocity field $\hat{u}_i$ (Pope, 2000; Olivieri *et al.*, 2022*b*). Integrating the resulting expressions from a finite wavenumber to infinity yields the spectral kinetic energy balance which, under statistically steady conditions, takes the form

$$\left\langle \Pi(\kappa) + \Pi_{\text{part}}(\kappa) + \mathscr{D}v(\kappa) \right\rangle_t = \langle \varepsilon \rangle_{\mathscr{V},t}\,, \tag{5}$$

where $\Pi(\kappa)$ denotes the nonlinear energy transfer, $\Pi_{\text{part}}(\kappa)$ the interphase exchange, and $\mathscr{D}_v(\kappa)$ the viscous dissipation.

Figure 3 reports these contributions as functions of κ/κ_L for representative values of M_p, with all quantities normalized by $\langle \varepsilon \rangle_{\mathscr{V},t}$. For reference, the unladen results for $\langle \Pi \rangle_t$ and $\langle \mathscr{D}v \rangle_t$ are also included as thin dashed lines. In the low-inertia case ($M_p = 0.1$), the magnitude of the nonlinear flux $\langle \Pi \rangle_t$ (red) closely matches that of the unladen flow, while the contribution of the particle-induced term $\langle \Pi\text{part} \rangle_t$ (yellow) remains weak. Consequently, the energy balance is governed primarily by nonlinear transfer and viscous dissipation across all scales. This indicates that the inertial cascade remains active for $\kappa/\kappa_L < 20$, in agreement with the $-5/3$ scaling observed in figure 2 (left).

In contrast, for the highest mass loading ($M_p = 0.6$), both the nonlinear transfer and viscous dissipation become negligible over large and intermediate scales, where the energy exchange is dominated by fluid-particle interactions. At the particle scale ($\kappa/\kappa_L = L/D$), the nonlinear contribution is essentially zero for all laden cases. At these scales, $\left\langle \Pi_{\text{part}} \right\rangle_t$ remains smaller than $\langle \mathscr{D}_v \rangle_t$ but increases markedly with M_p, while $\langle \mathscr{D}_v \rangle_t$ decreases. This trend, also observed by Schneiders *et al.* (2017, see figure 7 therein), is consistent with the short, nearly symmetric laminar wakes illustrated in the inset of figure 1 (right).

The combined evidence from the energy spectra in figure 2 and the scale-by-scale budget in figure 3 indicates that even small but sufficiently inertial particles can influence energy transfer at scales significantly larger than their size. While Kolmogorov-size particles with moderate M_p primarily affect the fine-scale structure of the flow, highly inertial suspensions substantially modify the large-scale dynamics. In this regime, the kinetic energy balance is dominated by fluid-particle coupling, and the nonlinear cascade becomes negligible, marking a strong departure from classical Kolmogorov turbulence.

Particle motion

Particle dynamics are strongly influenced by increasing inertia. As summarized in table 2, the magnitude of the particle velocity $\sqrt{\tilde{U}_i\tilde{U}_i}$ decreases as M_p increases. The particle statistics, including the mean $\langle\cdot\rangle_p$ and higher-order moments, are obtained by averaging over the ensemble of particles. The mean particle speed decreases as M_p increases from 0.1 to 0.4, and then remains approximately unchanged between $M_p = 0.4$ and $M_p = 0.6$, indicating that more inertial particles move more slowly in the frame of the computational domain. In a similar manner, the probability density function (PDF) of $\sqrt{\tilde{U}_i\tilde{U}_i}$ is computed by averaging over time. These PDFs exhibit an excellent collapse when expressed in terms of the Gaussian variable

Ψ_p	M_p	$\left\langle \tilde{U}_i\tilde{U}_i \right\rangle_p (F_0 L)^{-1/2}$
100	0.1	1.45 ± 0.11
250	0.2	1.28 ± 0.12
666	0.4	1.12 ± 0.10
1499	0.6	1.13 ± 0.09

Table 2: Mean and standard deviation of the absolute value of the particle velocity for increasing M_p.

$$Z = \frac{\sqrt{\tilde{U}_i\tilde{U}_i} - \left\langle \sqrt{\tilde{U}_i\tilde{U}_i} \right\rangle_p}{\sqrt{\left\langle \tilde{U}_i\tilde{U}_i \right\rangle_p - \left\langle \sqrt{\tilde{U}_i\tilde{U}_i} \right\rangle_p^2}}. \tag{6}$$

The inset in figure 4*a* demonstrates this collapse, indicating that the statistics of $\sqrt{\tilde{U}_i\tilde{U}_i}$ retain a Gaussian character for all values of M_p.

To further quantify particle transport, we examine the temporal evolution of the mean square displacement,

$$[R(t)]^2 = \langle (X_i(t) - X_i(0))\,(X_i(t) - X_i(0)) \rangle_p\,, \tag{7}$$

where X_i denotes the particle position. The results, shown in figure 4*b*, display a ballistic regime $[R(t)]^2 \sim t^2$ at short times $t \ll 1$, which is independent of M_p (dashed black line), consistent with previous findings for finite-size spherical particles (Chiarini *et al.*, 2024). In this representation, time is normalized by $(L/F_0)^{1/2}$ and displacement by L. For times $t = O(1)$, deviations from the ballistic regime become evident. At longer times, the cases with $M_p = 0.2$ and $M_p = 0.4$ tend toward the diffusive scaling $\sim t$, although they do not fully collapse onto the corresponding asymptote (solid line). By contrast, the most inertial case ($M_p = 0.6$, brown curve) does not exhibit a clear asymptotic regime, likely due to the limited duration of the available particle trajectories. Overall, the transition away from the ballistic regime occurs at progressively later times as particle inertia increases.

Particle clustering

In this section, we investigate how particle inertia influences clustering. Clustering is quantified via a Voronoi tessellation, whereby the Voronoi volume associated with each particle is defined as the region of space closer to that particle than to any other. Consequently, small Voronoi volumes correspond to locally concentrated regions, whereas large volumes identify more dilute areas (Monchaux *et al.*, 2010; Fiabane *et al.*, 2012). The propensity for clustering is assessed by comparing the PDFs of the Voronoi volumes obtained from the PR-DNS with those derived from a reference distribution of particles of diameter D, whose positions are assigned according to a random Poisson process (RPP).

The time-averaged PDFs of the Voronoi volumes $\mathscr{V}_{\text{voro}}$ from the simulations are shown in figure 5 for increasing mass fraction M_p (colored curves), alongside the RPP reference case

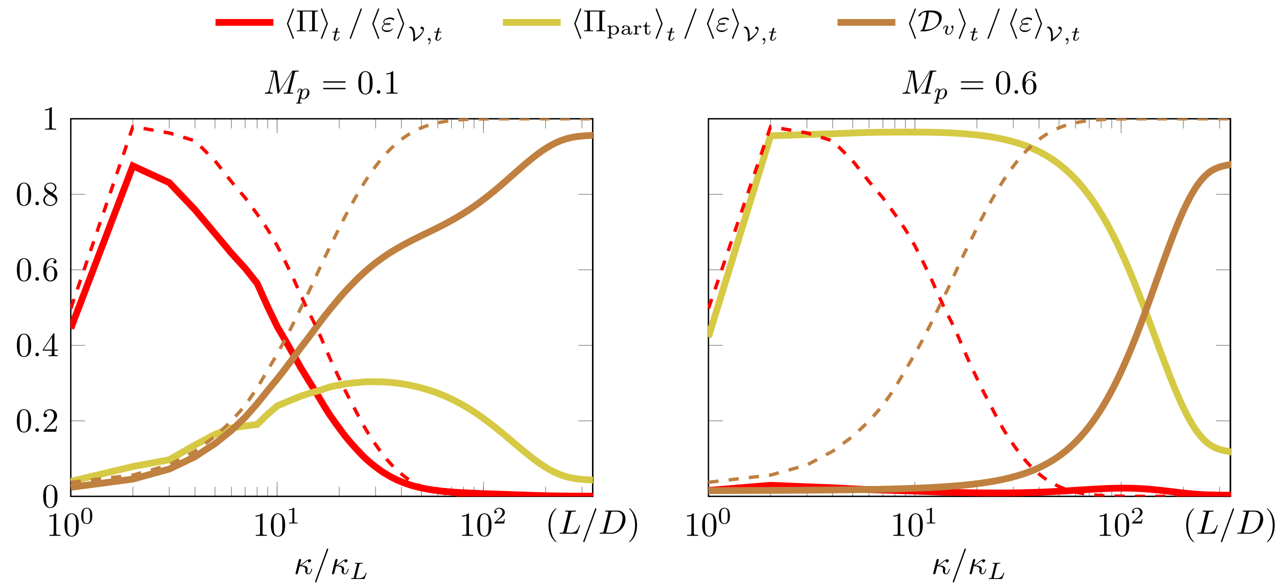

Figure 3: Terms of the normalised scale-by-scale energy budget (5) for increasing particle inertia. The thick, solid curves represent the turbulent transport term (red), particle forcing term (yellow) and dissipation term (brown) of the cases $M_p = 0.1$ (left) and $M_p = 0.6$ (right).

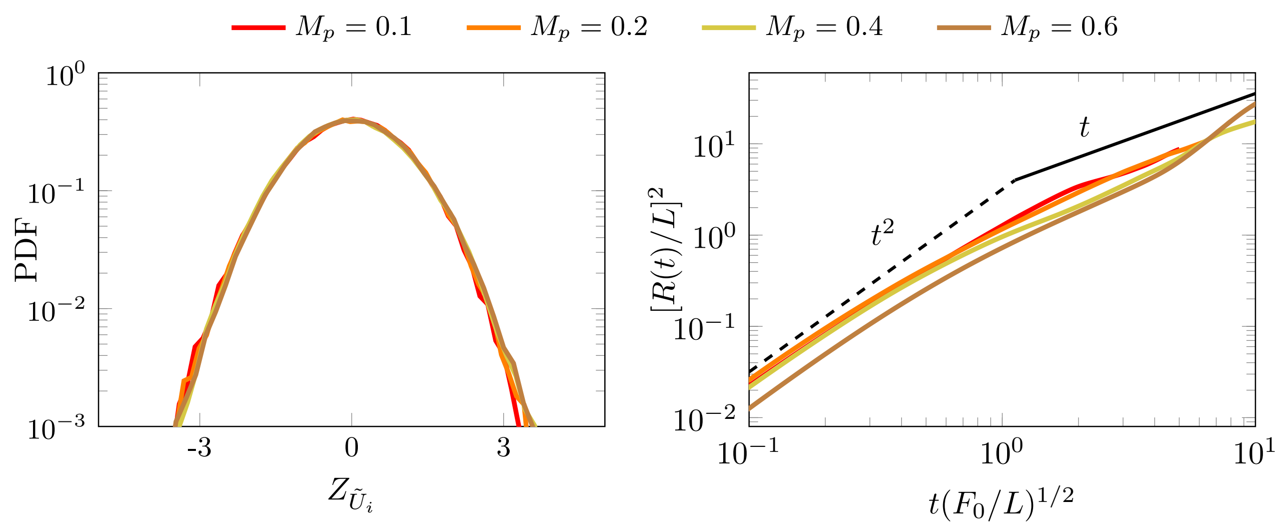

Figure 4: Left: PDF of the normalised absolute value of the particle velocity $Z_{\tilde{U}_i}$ (6). Right: mean square displacement $[R(t)]^2$ of the particles for increasing particle inertia (coloured curves). The results are compared with the scalings $[R(t)]^2 \sim t^2$ (black dashed line) and $[R(t)]^2 \sim t$ (black solid line).

(black curve) for N non-overlapping Kolmogorov-size particles. All PDFs are normalized by the inverse of the mean concentration, $\langle \mathscr{V}_{\mathrm{voro}} \rangle_{\mathscr{V}} = L^3/N = 1.35 \times 10^{-5}$. The deviation from the RPP distribution is most pronounced in the lightest case ($M_p = 0.1$, red). As both Ψ_p and M_p increase, the PDFs progressively approach the RPP limit, eventually collapsing onto it for $M_p = 0.6$. Since all distributions are normalized to unit mean, their broadening reflects the occurrence of both highly concentrated regions (small Voronoi volumes) and dilute regions (large volumes) relative to the random reference.

The standard deviation of the PDFs is largest for $M_p = 0.1$ and decreases monotonically as M_p increases, approaching the RPP value (black curve in figure 5) for the most inertial case. Accordingly, the likelihood of strong clustering events is highest at $M_p = 0.1$ and diminishes with increasing inertia. While the intermediate cases ($M_p = 0.2$ and $M_p = 0.4$) still exhibit moderate clustering, the distribution for $M_p = 0.6$ coincides with that of the RPP, indicating the absence of clustering. For an unladen flow at $Re_\lambda \cong 140$ and the same volume fraction $\Phi_p = 10^{-3}$, Chiarini *et al.* (2025) reported enhanced clustering as the density ratio Ψ_p increased from 5 to 100. The present results indicate an opposite trend when Ψ_p is further increased to values characteristic of gas–solid systems, $O(10^3)$ (Rose & Durant, 2009).

CONCLUSIONS

In summary, the present study demonstrates that increasing the inertia of Kolmogorov-size particles profoundly alters both the turbulent carrier flow and the particle dynamics.

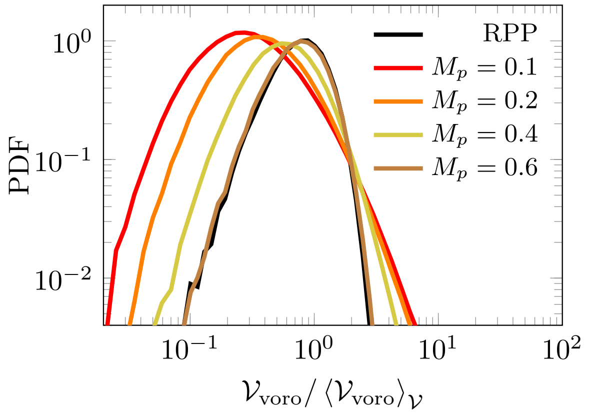

Figure 5: Left: PDFs of the normalised Voronoi volumes $\mathscr{V}_{\mathrm{voro}}/\langle \mathscr{V}_{\mathrm{voro}} \rangle_{\mathscr{V}}$ for increasing particle-to-fluid density ratio Ψ_p and mass fraction M_p are compared to that obtained for a suspension of finite-size particles distributed via a random-Poisson process (RPP, black).

While moderate mass loadings primarily affect the small-scale structure of the flow, high-inertia particles suppress the nonlinear energy cascade, leading to a regime dominated by fluid–particle interactions and viscous dissipation, with energy spectra departing significantly from classical Kolmogorov scaling. This transition is accompanied by a progressive decorrelation of the velocity field and a weakening of particle clustering, ultimately approaching a random spatial distribution at the highest mass fractions. These findings highlight the crucial role of particle inertia in modulating turbulence across scales, with implications for a wide range of particle-laden flows encountered in natural and industrial systems.

ACKNOWLEDGEMENTS

The authors acknowledge the computational resources provided by the Scientific Computing & Data Analysis Section of the Core Facilities at OIST and by HPCI under Research Project grants hp230536, hp250021, and hp250035. The research was supported by the Okinawa Institute of Science and Technology Graduate University (OIST) with subsidy funding to M.E.R. from the Cabinet Office, Government of Japan. M.E.R. also acknowledges funding from the Japan Society for the Promotion of Science (JSPS), grant 24K17210 and 24K00810.

REFERENCES

Arnold, V. I. 1965 Sur la topologie des écoulements stationnaires des fluides parfaits. *C. R. Acad. Sci. Paris* **261**, 17–20.

Brandt, L. & Coletti, F. 2022 Particle-laden turbulence: Progress and perspectives. *Ann. Rev. Fluid Mech.* **54** (Vol. 54, 2022), 159–189.

Chiarini, A., Cannon, I. & Rosti, M. E. 2024 Anisotropic mean flow enhancement and anomalous transport of finite-size spherical particles in turbulent flows. *Phys. Rev. Lett.* **132**, 054005.

Chiarini, A., Tandurella, S. & Rosti, M. E. 2025 Kolmogorov-size particles in homogeneous and isotropic turbulence. *J. Fluid Mech.* **1007**, A81.

Costa, P., Boersma, B. J., Westerweel, J. & Breugem, W.-P. 2015 Collision model for fully resolved simulations of flows laden with finite-size particles. *Phys. Rev. E* **92**, 053012.

Fiabane, L., Zimmermann, R., Volk, R., Pinton, J.-F. & Bourgoin, M. 2012 Clustering of finite-size particles in turbulence. *Phys. Rev. E* **86**, 035301.

Hori, N., Rosti, M. E. & Takagi, S. 2022 An Eulerian-based immersed boundary method for particle suspensions with implicit lubrication model. *Comput. Fluids* **236**, 105278.

Kim, J., Moin, P. & Moser, R. 1987 Turbulence statistics in fully developed channel flow at low Reynolds number. *J. Fluid Mech.* **177**, 133–166.

Marchioli, C., Bourgoin, M., Coletti, F., Fox, R. O., Magnaudet, J., Reeks, M., Simonin, O., Sommerfeld, M., Toschi, F., Wang, L.-P. & Balachandar, S. 2025 Particle-laden flows. *Int. J. Multiph. Flow* **191**, 105291.

Monchaux, R., Bourgoin, M. & Cartellier, A. 2010 Preferential concentration of heavy particles: A Voronoï analysis. *Phys. Fluids* **22** (10), 103304.

Olivieri, S., Cannon, I. & Rosti, M. E. 2022*a* The effect of particle anisotropy on the modulation of turbulent flows. *J. Fluid Mech.* **950**, R2.

Olivieri, S., Mazzino, A. & Rosti, M. E. 2022*b* On the fully coupled dynamics of flexible fibres dispersed in modulated turbulence. *J. Fluid Mech.* **946**, A34.

Pope, S.B. 2000 *Turbulent Flows*. Cambridge University Press.

Rose, W. I. & Durant, A. J. 2009 Fine ash content of explosive eruptions. *J. Volcanol. Geotherm. Res.* **186** (1), 32–39.

Rosti, M. E. 2026 Simulating laminar and turbulent multiphase flows with Fujin. *Fluid Dyn. Res.* **58** (2), 021401.

Schneiders, L., Meinke, M. & Schröder, W. 2017 Direct particle–fluid simulation of Kolmogorov-length-scale size particles in decaying isotropic turbulence. *J. Fluid Mech.* **819**, 188–227.

Tanaka, T. & Eaton, J. K. 2010 Sub-Kolmogorov resolution partical image velocimetry measurements of particle-laden forced turbulence. *J. Fluid Mech.* **643**, 177–206.

Tomé, M. F., Duffy, B. & McKee, S. 1996 A numerical technique for solving unsteady non-Newtonian free surface flows. *J. Non-Newton. Fluid Mech.* **62** (1), 9–34.

Tsuji, Y., Kawaguchi, T. & Tanaka, T. 1993 Discrete particle simulation of two-dimensional fluidized bed. *Powder Tech.* **77** (1), 79–87.